

# Functionalised SiO<sub>2</sub> Modified Icephobic Nanocomposite Electrospun Membranes for Outdoor Electromagnetic Shielding Applications

*Mahmut Tas<sup>1</sup>, Umar Gishiwa Musa<sup>1</sup>, Ifty Ahmed<sup>1</sup>, Fang Xu<sup>1</sup>, Christopher Smart<sup>2</sup>, and Xianghui Hou<sup>1\*</sup>*

<sup>1</sup>Advanced Materials Research Group, Faculty of Engineering, University of Nottingham, Nottingham, NG7 2RD, UK

<sup>2</sup>George Green Institute for Electromagnetics Research, University of Nottingham, University Park, NG7 2RD, UK

## **Abstract**

Outdoor electronic equipment such as signal stations, radar units, and cellular base stations would benefit from electromagnetic interference (EMI) shielding systems, but ice accretion on the surface of these facilities often causes critical challenges, especially in cold regions and winter season. In this study, icephobic nanocomposite electrospun membranes were developed via a two-step process from recycled polyethylene terephthalate (r-PET), which exhibited high electromagnetic shielding efficiency with superhydrophobic and icephobic performance. The surface superhydrophobicity and icephobicity of the membrane were achieved after surface modification using fluorinated silane functionalised SiO<sub>2</sub> nanoparticles (FSFS). Superhydrophobicity with less than 5° of contact angle hysteresis was observed on the nanocomposite electrospun membranes, and the ice adhesion strength was approximately 50 kPa after the FSFS modification, which was ~6 times lower than aluminium reference. Furthermore, with the addition of 20 wt% magnetite nanopowders, the r-PET nanocomposite electrospun membranes demonstrated a high magnetic response, around 4.22 emu/g, in the range of -10 and +10 kOe, and a high electromagnetic shielding efficiency between 11-22 dB in the frequency range of 400 MHz to 6 GHz. The icephobic r-PET electrospun membranes incorporated with magnetite are promising candidate materials for outdoor EMI shielding applications.

**Keywords:** Outdoor EMI shielding materials; icephobic fibrous surfaces; electrospun nanocomposite fibres

## 1. Introduction

Outdoor electronic facilities, such as signal stations, radar units, and cellular base stations, play essential roles in modern human life to provide safety and communication. One critical issue of these electronic facilities is their potentials to emit electromagnetic radiation. Some studies have linked long-term exposure to electromagnetic waves with cancer, childhood leukemia, central nervous system disorders, and depression<sup>1-4</sup>; thus, electromagnetic pollution is of relevant concern to the public. Therefore, Electromagnetic interference shielding is a prominent feature that finds applications in many industries (i.e., aircraft, satellites<sup>5-7</sup>).

Another key challenge for outdoor electronic facilities is ice accretion on the surface, especially in cold regions and winter season, which may significantly affect their functionalities, reduce the efficiency and shorten the service life. Although several publications investigated new materials for outdoor EMI shielding applications<sup>8-10</sup>, no study has been found which considered ice mitigation while designing their materials. There are some attempts considering the combination of superhydrophobicity and EMI shielding efficiency in a single material system. Ma *et al.* prepared multifunctional polyvinylidene fluoride/carbon (graphene and multi-walled carbon nanotube) porous composite materials and reported electromagnetic shielding efficiency of 28.5 dB at a frequency of 8-12 GHz. They also evaluated the superhydrophobicity of these materials which had water contact angles (WCA) of 155°<sup>8</sup>. Megaridis *et al.* prepared polytetrafluoroethylene/carbon nanofibre nanocomposites and reported EMI shielding efficiency of 25 dB in the range of 8.2–12.4 GHz along with WCA up to 158°<sup>9</sup>. Ma *et al.* treated cotton fabrics with Nafion/multi-walled carbon nanotube dispersions, which achieved 9 dB EMI shielding efficiency along with WCA of 154°<sup>11</sup>. Lee *et al.* reported surface-modified carbon nanotube films that achieved a contact angle of 153° and sheet resistance of  $4.1 \times 10^4 \Omega/\text{square}$ <sup>12</sup>, suggesting their potential application for electromagnetic shielding. Zhai *et al.* prepared nanocomposite coatings using carbon nanotubes

with conjugated block co-polymer (rrP3HT-b-PS), which had electrical conductivity of 30–100 S cm<sup>-1</sup> and a contact angle of above 158°<sup>13</sup>. Although the above work reported impressive progress in EMI shielding materials with hydrophobic surface, the icephobic performance have not been studied.

Electrospinning, as a versatile nanofibre production method, has attracted significant attention in the past decades due to the excellent properties of the electrospun fibres, such as large specific surface area, high porosity, flexibility, adjustable fibre diameters and tuneable wettability<sup>14, 15</sup>. The randomly oriented fibrous structure and high amount of air pockets on the surface make them strong candidates for icephobic applications considering Cassie-Baxter icing state. Moreover, polymer-based EMI shielding composites have become popular alternatives for the replacement of traditional metal-based EMI shielding materials, due to their advantages of easy processability, lightweight nature and corrosion resistance<sup>16</sup>. It is also believed that thin nanofibrous membranes are promising for EMI shielding applications because of to their porous structures which lead to an increase in multi-reflection loss<sup>17</sup>. Additionally, the use of electrospinning process to fabricate nanocomposite fibre membranes allows to impart specific properties such as high dielectric constant which is an important factor for EMI shielding<sup>17, 18</sup>.

Polyethylene terephthalate (PET) is one of the most widely produced thermoplastic polymers which has been used as textiles (e.g. yarns<sup>19</sup> and fabrics<sup>20</sup>), in the food industry (e.g., bottles, packing<sup>21</sup>), and for electrical applications (such as insulator materials<sup>22</sup>). Disposable products such as bottles and packaging comprise the major composition of PET. However, only a relatively small amount of PET products has been recycled<sup>23, 24</sup>. As such, exploring alternative recycling approaches for PET would help to address the associated economic and environmental concerns.

In the present work, nanocomposite electrospun membranes combining icephobicity and EMI shielding efficiency have been developed via a two-step process from recycled polyethylene terephthalate (r-PET), as promising candidate materials for outdoor EMI shielding applications. Magnetite/r-PET nanocomposite nanofibre membranes were produced by electrospinning process, followed by surface modification with fluorinated silane functionalised SiO<sub>2</sub> (FSFS) nanoparticles. The superhydrophobic and icephobic properties of the as-prepared membranes were evaluated. Furthermore, with the incorporation of magnetite nanopowders, the r-PET nanocomposite electrospun membranes demonstrated a high magnetic response, and their EMI shielding performance was studied.

## **2. Materials and Experimental Methods**

### **2.1 Materials**

Recycled PET coke bottles were cut into small pieces to prepare r-PET solution for electrospinning. Acetone (>99.9 wt%) and ethanol (>99.9 wt%) were used to clean the PET pieces. Trifluoroacetic acid (TFA) (>99 wt%) and dichloromethane (DCM) (>99.8 wt%) were selected as the solvents of r-PET to prepare the electrospinning solution. For the fabrication of magnetite-loaded r-PET electrospun membranes, magnetite nanopowder (<100 nm particle size, Sigma Aldrich, UK) was used. A fluorinated silane coupling agent, 1h,1h,2h,2h-Perfluorooctyltriethoxysilane (PFOTES) (98 wt%, Sigma Aldrich, UK) was used for the preparation of FSFS with fumed SiO<sub>2</sub> (Aerosil R 805, 5-20 nm). Sodium hydroxide (Alfa Aesar) was chosen to activate the fibre surface prior to the FSFS treatment.

### **2.2 Preparation of r-PET solutions**

The r-PET pieces were first washed with acetone and ethanol, using an ultrasonic bath for 15 min each, respectively. The r-PET pieces were then dissolved in a mixture of TFA and DCM

(1:1 by volume), to form 15 wt% solution. The blended solution was vigorously mixed with a magnetic stirrer for 4 hours at room temperature. To obtain a homogenous nanocomposite nanofibre membrane, it was important for magnetite to stay stable and not precipitate in the dispersion. During solution preparation step, we trialed several concentrations and 20 wt% of magnetite with respect to PET amount was the highest concentration we could achieved for a stable dispersion. Thus, for the preparation of r-PET/magnetite dispersion, 20 wt% magnetite with respect to polymer amount was dispersed in the TFA/DCM solution using an ultrasonic probe for 15 minutes. Then, 15 wt% of r-PET was eventually added to the magnetite dispersion and stirred for 4 hours. The r-PET/magnetite solution was finally subjected to ultrasonication for 30 minutes before the electrospinning process. All the procedures were carried out in a fume hood because of the high volatility of the solvents used.

### **2.3 Fabrication of r-PET and magnetite/r-PET nanocomposite electrospun membranes**

An in-house electrospinning rig with a rotating drum collector was used to fabricate electrospun membranes. The detailed setup has been reported elsewhere<sup>25</sup>. 10 ml of the prepared dispersion was loaded into a 20 ml syringe and then attached to a syringe pump. A constant flow rate of 2 ml/h, a high voltage of 17.5 kV, and a collector-needle distance of 13 cm were used for all membranes, and approximately 200  $\mu\text{m}$  of membrane thickness was achieved for each sample. All samples were dried in a 50 °C oven overnight before further characterisation.

### **2.4 Preparation of FSFS and Surface Treatment of Electrospun membranes**

To prepare FSFS, PFOTES was used as a silane coupling agent. Briefly, 0.1 ml ammonium hydroxide, 1 ml distilled water and 1 ml PFOTES were added into 10 ml ethanol and stirred for 1 hour at 60 °C. Then, 0.1 g  $\text{SiO}_2$  with an average size of 5-20 nm was dispersed into the solution and mixed for another 3 hours at 60 °C. After that, the prepared FSFS was centrifuged

at 9000 rpm for 10 min, supernatant was discarded, and nanoparticles were dispersed in hexane. As the prepared FSFS nanoparticles tended to aggregate fast in water or aqueous suspensions, hexane was used to disperse FSFS nanoparticles which offered reasonably stable dispersions for dip coating process.

The schematic representation of the fluorination process is given in Figure 1.

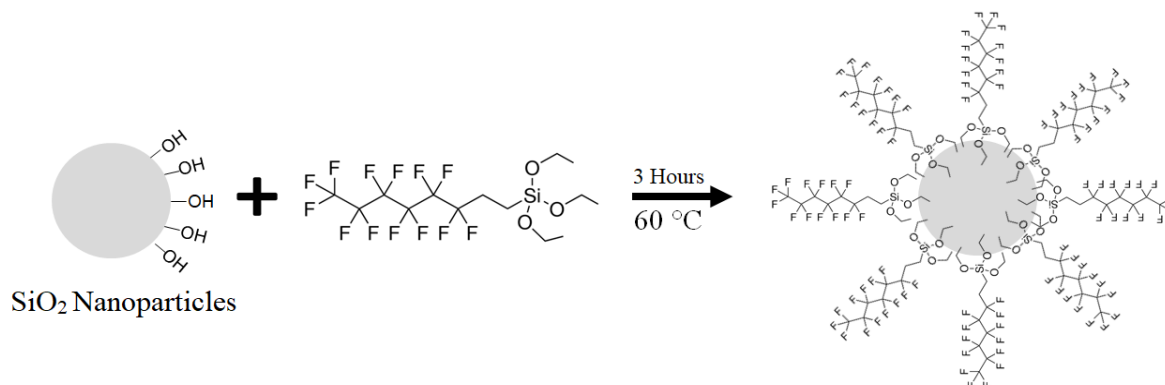


**Figure 1.** Surface modification of SiO<sub>2</sub> nanoparticles with PFTOES.

For the surface treatment of electrospun membranes, it was essential to form stronger attractions between the fibre surface and the FSFS nanoparticles. Therefore, the surface activation process was conducted using 0.1 M NaOH aqueous solution to create functional groups on the surface of electrospun fibres. The samples were then washed with distilled water and dried in an oven at 50 °C. After that, the electrospun membranes were immersed in the hexane solution consisting of 5mg/ml FSFS particles for 5 seconds followed by heating at 120 °C for 1 hour <sup>26</sup>.

## 2.5 Characterisation

### 2.5.1 FTIR and XPS Analysis

FT-IR analysis of the SiO<sub>2</sub>, PFOTES, and FSFS were conducted using a Perkin Elmer FT-IR spectrometer with Attenuated Total Reflection (ATR) between 650 and 2000 cm<sup>-1</sup> to understand the reaction mechanism of PFOTES and SiO<sub>2</sub>. After the preparation of the FSFS

treated r-PET/magnetite nanocomposite membranes, XPS analysis was performed to investigate the chemical composition of the sample, using a VG ESCALab Mark II X-ray Photoelectron Spectrometer.

### **2.5.2 Surface Morphology and Topography**

An electrically conductive iridium layer was applied to the sample surface using Quorum Sputter Coater, Q150R. before morphological study. A Joel 7000F scanning electron microscope (SEM) was used to investigate the surface morphologies of the samples, and ImageJ was utilised to calculate average fibre diameters and their distributions from a total of 50 measurements. Moreover, energy dispersive spectroscopy (EDX) which were attached the SEM was used to investigate the distribution of magnetite nanoparticles. The surface topography of the magnetite/r-PET and FSFS treated magnetite/r-PET samples were analysed using a 3D profilometer, Zeta-20. The area of each measurement was 120  $\mu\text{m}$  x 90  $\mu\text{m}$ .

### **2.5.3 Surface Wettability**

FTA200 dynamic contact angle system was used to investigate the static, advancing, and receding contact angles of the samples. The static and dynamic contact angle values were determined using a droplet volume of 4  $\mu\text{l}$ , while sliding contact angles were determined according to tilted plate experiments using a droplet volume of approximately 10  $\mu\text{l}$ . The contact angle hysteresis of the samples was calculated using Eq. 1.

$$\theta_{hyst} = \theta_{adv} - \theta_{rec}; \quad (Eq.1)$$

where  $\theta_{hyst}$  is the contact angle hysteresis,  $\theta_{adv}$  is the advancing contact angle and  $\theta_{rec}$  is the receding contact angle.

### **2.5.4 Ice Adhesion Strength**

Ice adhesion tests were performed using a centrifuge method <sup>27, 28</sup>. A 2 g glaze ice block was developed on the sample surface in a -10°C chamber using distilled water to measure ice adhesion strength. The ice adhesion strengths were calculated using Eq. 2.

$$\tau = \frac{mr\omega^2}{A} \quad (Eq. 2)$$

where  $\tau$  is ice adhesion strength,  $\omega$  is the rotational speed at the detachment of the glaze ice block,  $m$  is the mass of the ice (kg) and  $r$  is the radius of the beam (m) and  $A$  is the contact area of ice/solid surface (m<sup>2</sup>) <sup>29</sup>.

### 2.5.5 Electromagnetic Shielding Efficiency and Magnetic Hysteresis Measurements

Electromagnetic shielding efficiency measurement of the samples was carried out using a flanged coaxial EMI shielding effectiveness (SE) tester which was custom-built based on ASTM D4935-99 to obtain a wide range of measurements of smaller-sized samples <sup>30</sup>. The schematic diagram of the setup with a photo of fabricated holder is available from the supporting information Figure S1).

The diameter of the samples for EMI shielding measurement was 30 mm and approximately 1.5 mm thick layer was obtained with a few plies of the prepared membranes for the subsequent measurement. A vector network analyser (Agilent E8362B) was used to detect the  $S_{21}$  parameter at a frequency range of 400 MHz to 6 GHz.

Electromagnetic shielding efficiency were presented in decibel (dB) and percentages. The total shielding efficiency of the samples in dB values was calculated using Eq. 3:

$$SE_{dB} = 10 \log_{10}(1/[S_{21}]^2) \quad (Eq. 3)$$

Additionally, dB values could be converted to percentages using Eq.4.

$$SE_{\%} = (1 - 10^{-SE_{dB}/10}) \times 100 \quad (Eq. 4)$$

Where  $SE_{\%}$  is the shielding efficiency in percentage and  $SE_{dB}$  is the shielding efficiency in Decibels.

### **3. Results and Discussion**

#### **3.1 Morphological Characterisation**

SEM images of r-PET and r-PET/magnetite nanocomposite membranes are shown in Figure 2. The average fibre diameter of the r-PET electrospun membrane was  $372 \pm 132$  nm and the majority of the fibres were between 150 and 550 nm in diameter. However, the addition of magnetite to the polymer revealed a dramatic change in the distribution of fibre diameters. Although the average fibre diameter of magnetite/r-PET was within the error ( $248 \pm 124$  nm), the majority of the fibres had a reduced diameter between 50 and 350 nm, affected by the addition of magnetite nanoparticles. This change was attributed to whipping instability related to surface tension and the viscosity of the polymer solution. The whipping instability of the polymer jet changed due to the variation of the surface tension and surface charge repulsion. The viscosity of the solution also altered due to the incorporation of magnetite nanoparticles which triggered the electrified liquid jet to split into smaller branches during the electrospinning process<sup>31</sup>.

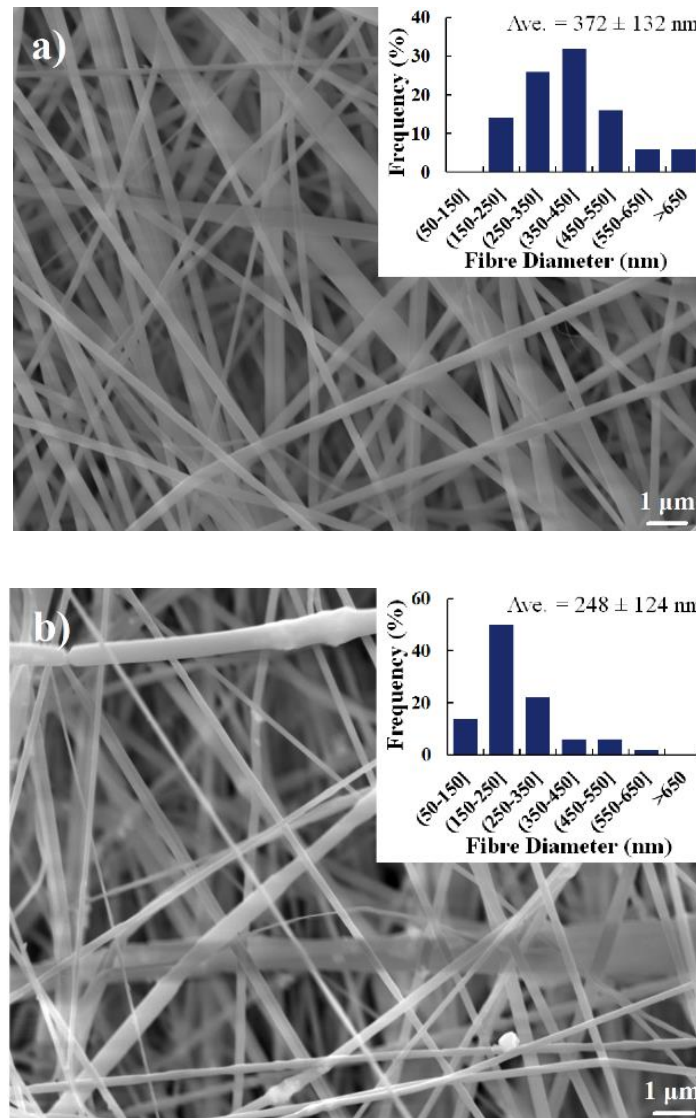


**Figure 2.** SEM images of (a) pure r-PET and (b) r-PET/magnetite nanocomposite fibre membrane (inset images: fibre diameter distributions of the samples)

Although there was a significant colour change from white (r-PET) to black (r-PET/magnetite nanocomposites) with the addition of 20 wt% of magnetite inside the polymer, as a result of solution mixing, magnetite nanoparticles mainly were incorporated inside the fibres. Even though probe sonication was used to agitate the magnetite nanoparticles thoroughly, some agglomerated particles were observed, most likely caused by the high surface energy and high concentration of the particles. However, the effect of these agglomerated particles on the surface properties was limited as they did not cause an elemental heterogeneity but only a

restricted morphological change. When the polymer and nanoparticles are mixed together homogeneously, theoretically, nanoparticles would be incorporated inside the fibres or at least covered by a polymer layer after solvent evaporation (Figure 3), which provide an elementally homogenous electrospun surface in both cases.

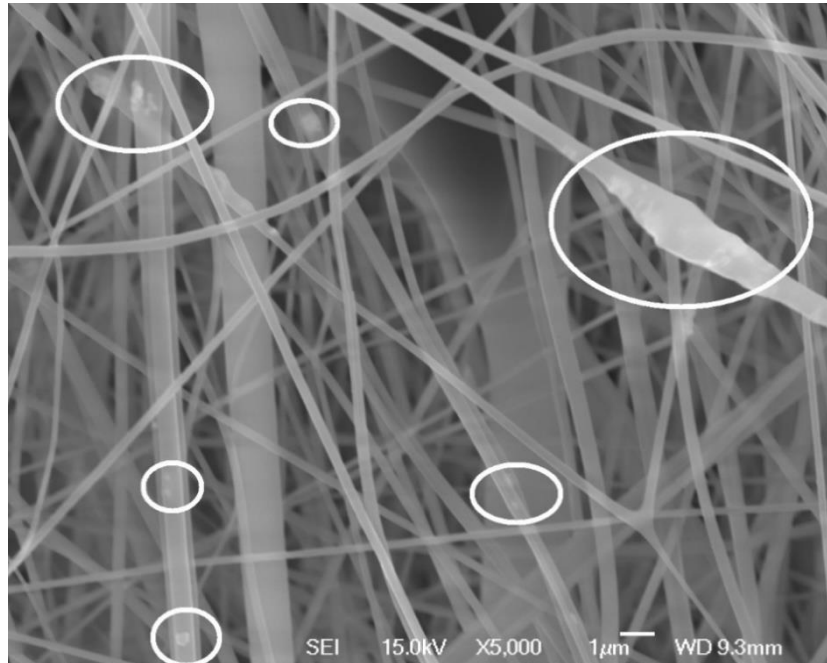


**Figure 3.** Agglomerated magnetite nanoparticles and their effect on morphology of the electrospun membrane (circles: agglomerated magnetite nano particles).

After the dip coating with FSFS was carried out, both the surface chemistry and morphology had been changed significantly. The SEM image of the FSFS coated r-PET/magnetite nanofibre membrane is given in Figure 4. As observed, the FSFS nanoparticles were accumulated on the surface of the fibres. This surface structure was favourable to achieve superhydrophobicity by not only the change on the surface chemistry but also the hierarchical structure. Electrospun nanofibre membrane already has a rough "fibre-scale" surface because of the randomly oriented fibres, while the addition of nanosized FSFS on the surface provided a much lower scale roughness.

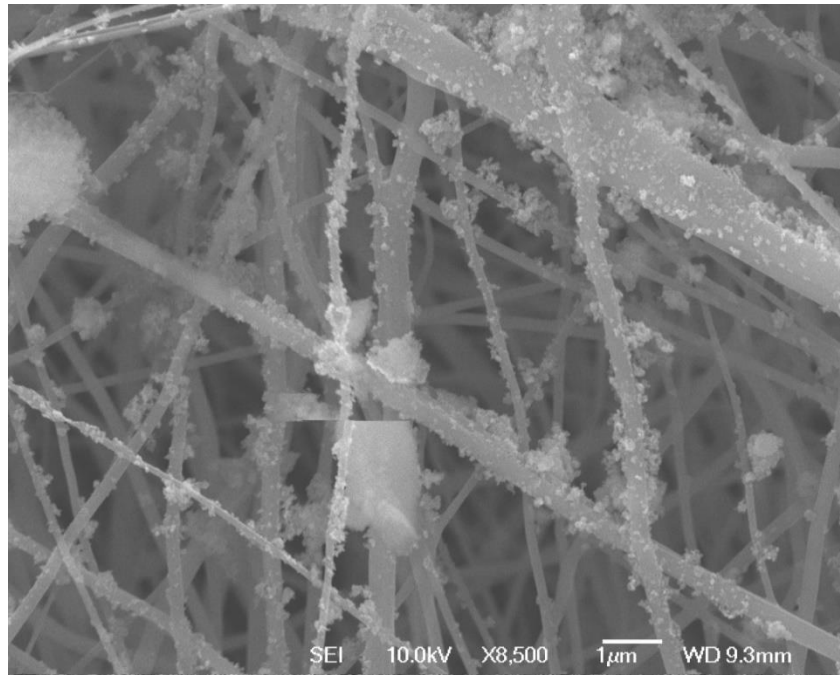


**Figure 4.** SEM image of FSFS coated r-PET/magnetite nanofibre membrane

The surface appearance and topographical images of the r-PET nanofibre membrane before and after the FSFS treatment are shown in Figure 5. As the method used for topographical images was microscale, it did not show a significant difference after the FSFS treatment which introduced nanoscale changes. The randomly distributed fibres, different diameters, and the presence of FSFS particles had majorly contributed to the roughness of the electrospun membranes.

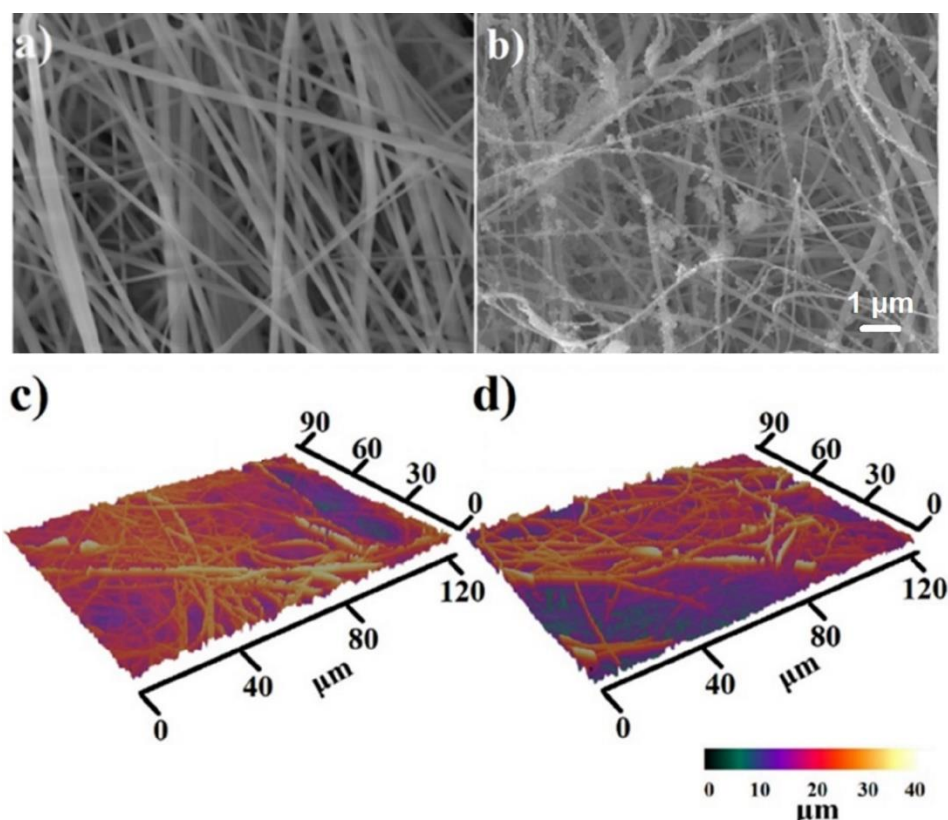


**Figure 5.** SEM and 3D topographical images of (a and c) r-PET/magnetite nanocomposite fibre membrane and (b and d) FSFS treated r-PET/magnetite nanocomposite fibre membrane.

### 3.2 Spectroscopic analysis

FT-IR spectra of SiO<sub>2</sub>, PFTOES, and FSFS are shown in Figure 6 over a wavenumber range of 650-2000 cm<sup>-1</sup>. The main peaks expected from SiO<sub>2</sub> were Si-O-Si and Si-O peaks in this range as there is no other chemical bonding in the structure of SiO<sub>2</sub>. Si-O-Si stretching, and Si-O bending bands were observed at around 1080 and 802 cm<sup>-1</sup>, respectively<sup>32,33</sup>. In the spectrum of PFTOES, characteristic peaks of CF<sub>2</sub> and CF<sub>3</sub> were found between 1325 and 1100 cm<sup>-1</sup><sup>34</sup>. Even though the Si-O-Si band and the characteristic peaks of PFTOES occurred in the same region, leading to the overlapping of the peaks, the spectrum of FSFS reaffirmed that SiO<sub>2</sub> particles had been successfully fluorinated.

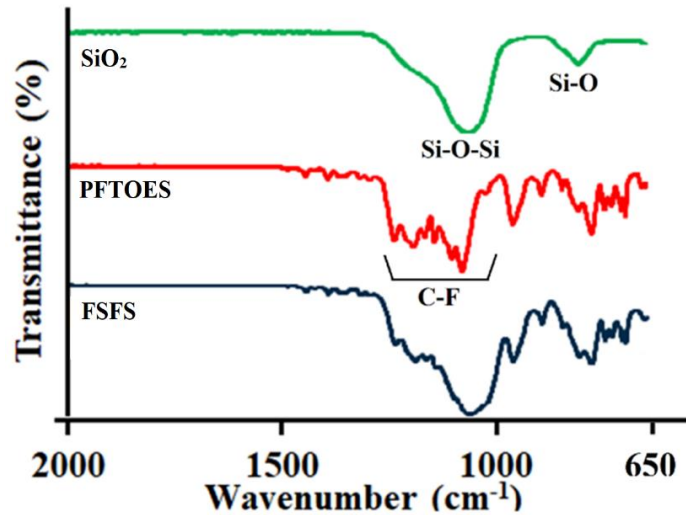


**Figure 6.** FT-IR spectra of SiO<sub>2</sub>, PFTOES, and FSFS

EDX mapping images of r-PET/magnetite and XPS spectrum of FSFS treated r-PET/magnetite are shown in Figure 7. The EDX mapping results revealed homogenous distribution of iron from the measurement of the nanocomposite fibres. The XPS spectrum confirmed the F and Si presence on the surface of the FSFS treated r-PET/magnetite electrospun sample. According to Figure 7b, Si peaks were found at 155 eV and 104 eV, referring to Si 2s and Si 2p, respectively. Because the sample with FSFS coating was not a flat thin film but had relatively heterogenous nano-granular surface roughness, the intensities of the peaks are disregarded. It is also noteworthy that according to the XPS results, the content of the Fe on the surface is ignorable, indicating that the magnetite particles were incorporated inside the fibres, or at least covered with a polymer layer during solution mixing. Otherwise, a dominant peak of Fe would appear.

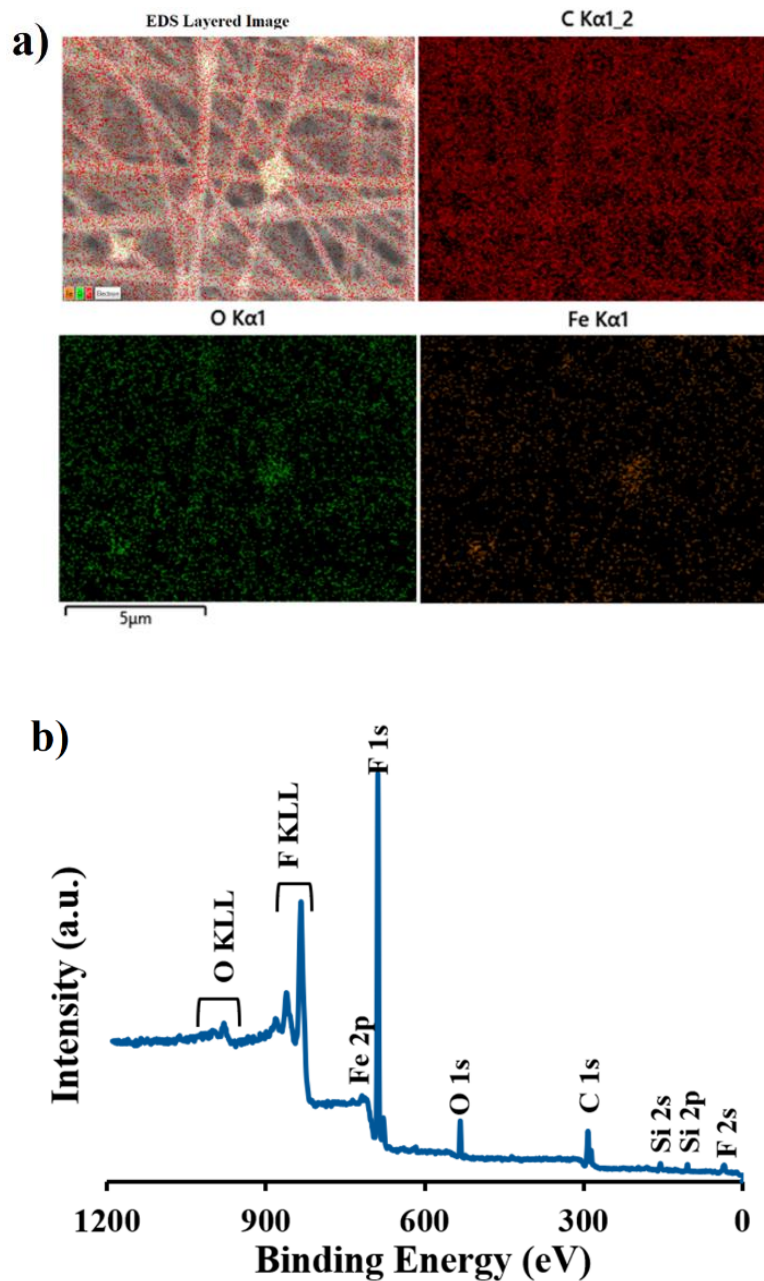


**Figure 7.** (a) EDX mapping image of r-PET/magnetite nanocomposite fibres and (b) XPS spectrum of FSFS treated r-PET/magnetite nanocomposite fibres

### 3.3 Surface Wettability

Static, advancing and receding contact angle (CA) values of the samples before and after FSFS treatment are highlighted with their CA hysteresis in Table 1. r-PET and magnetite/r-Pet

nanocomposite electrospun membrane exhibited similar wetting behaviour with water contact angles of 137.8 and 137.6° respectively, and the addition of magnetite only had a minimal effect on the wetting behaviour of the samples. It was because the majority of the magnetite nanoparticles were incorporated inside the fibres, not on the surface which had been proofed by XPS spectrum and SEM images. As such, the chemical composition of the surface of r-PET/magnetite sample remained similar to that of the r-PET. Also, although a difference in fibre diameter distribution between r-PET and r-PET/magnetite nanofibre membranes was observed, it was insufficient to affect surface wettability. The samples without FSFS treatment showed high static contact angles (higher than 133°), indicating hydrophobic surfaces. However the contact angle hysteresis of the samples was higher than 46° which indicated that mobility of the droplet was significantly limited as a result of high surface tension of PET (44.6 mJ/m<sup>35</sup>). Therefore, no sliding angle could be measured for samples without FSFS treatment, as the droplets were pinned to the surface regardless of the tilt angle.

**Table 1.** Static, advancing, and receding CA values of r-PET, magnetite/r-PET, and FSFS treated magnetite/r-PET samples with their CA hysteresis and sliding angles.

<b>Sample</b>	<b>Static CA (°)</b>	<b>Advancing CA (°)</b>	<b>Receding CA (°)</b>	<b>CA Hysteresis (°)</b>	<b>Sliding Angle (°)</b>
<b>r-PET</b>	137.8±2.6	136.3±1.2	82.6±3.2	55.6±3.0	>90°
<b>20% mgt/rPET</b>	137.6±0.1	133.3±0.4	86.6±2.5	46.6±2.6	>90°
<b>FSFS treated 20% mgt/r- PET</b>	N/A*	158.2±3.3	154.6±4.2	3.8±3.7	<1°

\* Exceptional superhydrophobic surface, water contact angle was difficult to be measured, due to the immediate bouncing and moving of the water drops.

Surface chemistry and surface topography are the two major factors in identifying the wetting behaviour of the materials. Fibrous materials are already reported as good candidates for superhydrophobic applications due to their naturally occurring rough structure<sup>36</sup>. After the FSFS treatment, the samples displayed exceptional superhydrophobicity which was most likely due to the dramatic change in both surface chemistry and morphology. The static contact angle of the FSFS treated sample could not be measured because of the immediate ‘rolling-off’ of the droplet from the surface. However, as the droplet stayed pinned to the needle in the method of dynamic contact angle measurements, it was possible to evaluate the advancing and receding contact angles which were used to calculate the CA hysteresis. The FSFS treatment resulted in a significant decrease in the surface energy of the final structure compared to the r-PET electrospun membrane. Moreover, the FSFS nanoparticles on the fibres contributed to a hierarchical surface structure, which also played a vital role in surface wettability. The combination of these changes drastically improved the surface hydrophobicity in terms of contact angle and contact angle hysteresis. The FSFS treatment also changed the wetting state of the sample. The droplet did not penetrate between the fibres but sit on the air pockets which is known as Cassie-Baxter state.

### **3.5 Ice Adhesion Strength**

To compare the ice adhesion strengths, an Al plate (used as a reference) and r-PET, FSFS treated r-PET, and FSFS treated r-PET/magnetite samples were all subjected to centrifuge testing. However, it was found that without the FSFS treatment, the r-PET was damaged during the ice adhesion strength test, most likely whilst the ice was detaching from the surface (see

inset Figure 8a). Basically, it was because the adhesion between ice and the electrospun membrane was higher or localised ice interlocking occurred on the membrane surface.

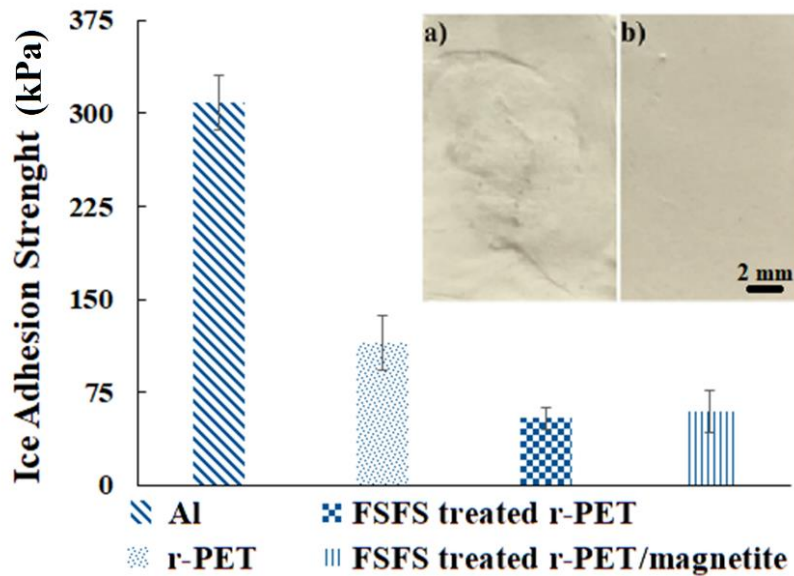


**Figure 8.** Ice adhesion strengths of the aluminum reference versus r-PET, FSFS treated r-PET and FSFS treated r-PET/magnetite electrospun membranes (inset: Surface appearance after ice adhesion test for (a) untreated and (b) FSFS treated samples)

There are two leading states when water droplets contact rough surfaces (i) Cassie-Baxter state and (ii) Wenzel State. In the Cassie-Baxter state, the droplet of water sits on top of the rough structures and air pockets, while in the Wenzel State, the water droplet thoroughly wets the rough structures<sup>37</sup>. The samples without FSFS treatment showed the Wenzel state when contacting water, which resulted in water penetration into the air gaps between the fibres. Moreover, whilst ice accretion occurred, it may be locally anchoring inside the nanofiber membrane, within the space between the fibers, causing high ice adhesion due to potential mechanical interlocking at the ice-surface interface. The surface fibers in the ice interlocking regions may have been seriously deformed or broken, leading to the damage of the surface fibrous structure (Figure 9).

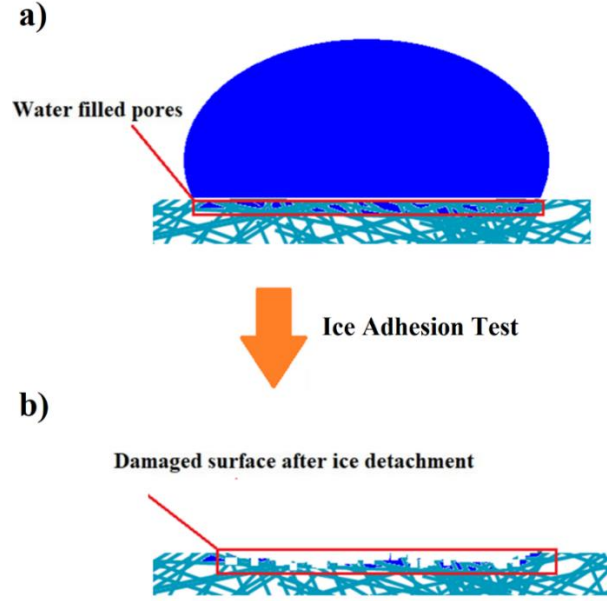


**Figure 9.1** The effect of Wenzel State on the surface damage during the ice-adhesion test for untreated *r*-PET/magnetite nanofibre membranes, (a) before and (b) after ice adhesion test

Additionally, the state of wetting has a critical role at the icing interface between ice and nanofibre membrane. The work of adhesion in Wenzel state ice can be explained using the following equation:

$$W_{sl}^W = r \cdot W_{sl}^{smooth} \quad (Eq.5)$$

Where  $W_{sl}^W$  is work of adhesion in Wenzel state,  $r$  is the ratio of actual surface area to the apparent one, and  $W_{sl}^{smooth}$  is the work of adhesion for a smooth surface. Because  $r$  is larger than 1 according to the Wenzel state, the work of adhesion increases significantly. However, an opposite situation will take place in Cassie-Baxter state, which can be summarised using the following equation:

$$W_{sl}^{CB} = r_f \cdot f \cdot \sigma_{lv} (1 + \cos\theta_{sl(r)}^{smooth}) = r_f \cdot f \cdot W_{sl}^{smooth} \quad (Eq.6)$$

Where  $W_{sl}^{CB}$  is the work of adhesion in Cassie-Baxter state,  $f$  is the wetted area, and  $r_f$  is a roughness factor of the wetted area. As  $r_f$  is significantly lower in the Cassie-Baxter state than the smooth surface contact area, the work of adhesion would decrease<sup>38</sup>. The schematic representation of the influences of the wetting states on the cross-sectional area at the ice-substrate interface is described in Figure 10.

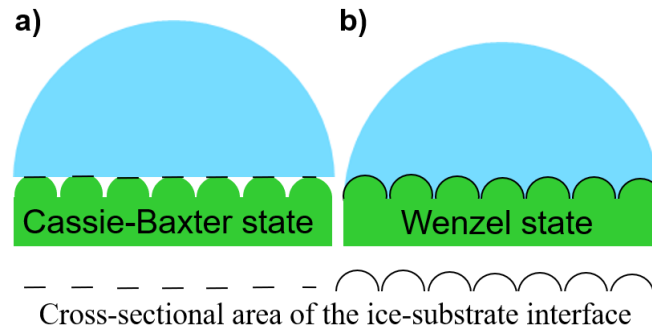


**Figure 10.** The influences of (a) Cassie-Baxter state and (b) Wenzel state at the interface between ice-fibre membrane

It is also possible that high surface tension and high contact angle hysteresis contribute to a high adhesion strength. About 105 kPa ice adhesion strength was obtained for the samples without FSFS treatment. However, due to the damage of the surfaces, the actual ice adhesion strength of the samples without FSFS treatment was expected to be even higher.

Similar results were observed by Varanasi *et al.*<sup>39</sup>. They reported that Wenzel ice had much higher ice adhesion strengths due to the frozen form of the water within the air pockets. Additionally, after FSFS treatment, the surface showed much lower contact angle hysteresis and better droplet repellence which may also contribute to the decrease of the ice adhesion strength. Farnezh *et al.*<sup>40</sup> found that a high contact angle hysteresis, which points to Wenzel State, resulted from a high ice adhesion strength due to a large ice-solid area upon icing. Chen *et al.* prepared superhydrophobic sol-gel coatings on glass substrates and reported low ice

adhesion strength down to 75 kPa with stable Cassie ice state <sup>41</sup>. Kulinich *et al.* investigated the relationship between water contact angle and ice adhesion strength when the Cassie-Baxter state took place <sup>42</sup>. A strong reverse-correlation between water contact angle and ice adhesion strength was obtained when the surface exhibited Cassie-Baxter wetting state and approximately 50 kPa of ice adhesion was achieved when high water contact angle surfaces were used. Linker free fluoropolymer coated Si substrates were also prepared to achieve low ice adhesion strength, and the structure demonstrated Cassie-Baxter state and exhibited high receding contact angles and low contact angle hysteresis <sup>43</sup>. Ice adhesion strength of 185 kPa was reported, approximately six times lower than bare Si substrate.

The fibrous materials can be good candidates for anti-icing applications <sup>36</sup>. Farhadi *et al.* <sup>44</sup> investigated the anti-icing properties of superhydrophobic nonwoven fabrics and they found that fibrous structures were promising to achieve Cassie-Baxter state. As comparison, we have achieved good icephobicity using a scalable electrospinning technique which may widen the horizon of polymer-based fibrous icephobic surfaces. Moreover, it has been proved that fibrous material structure has good capability to achieve Cassie-Baxter surface wetting state and lower the surface-water interaction due to the presence of air pockets, which prompting its anti-icing performance.

### **3.6 Magnetisation and Electromagnetic Shielding Efficiency**

The effect of magnetite incorporation on the magnetisation properties was investigated at room temperature and the results are shown in Figure 11. With 20 wt% magnetite, a high saturation magnetisation with approximately 4.22 emu/g was obtained. It indicated that although strong solvents (TFA and DCM ) and the multistep process were used for the preparation of the samples, the magnetic properties of magnetite nanoparticles had not been affected which is a critical requirement for the electromagnetic shielding efficiency.

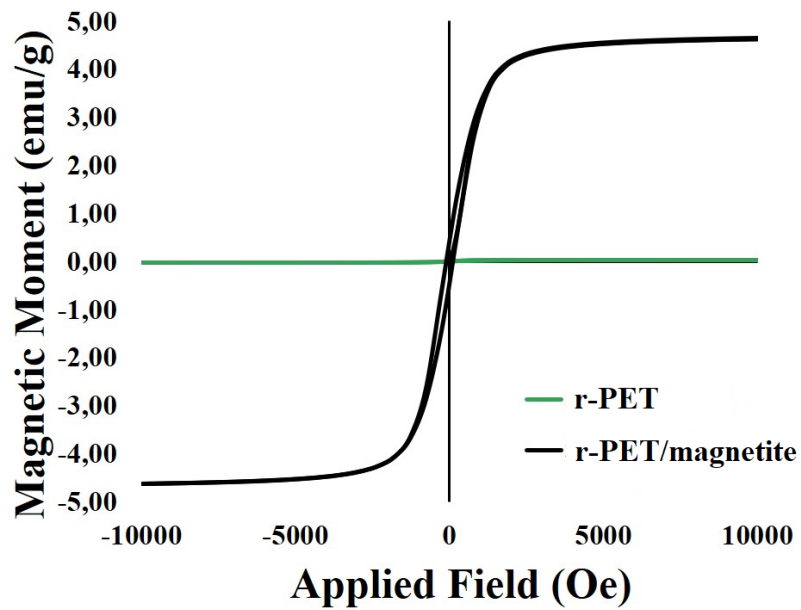


**Figure 11.** Magnetic hysteresis of the r-PET and r-PET/magnetite electrospun samples

$S_{21}$  parameter was used to investigate the shielding efficiencies of the samples which represents the power transferred from Port 2 to Port 1. The electromagnetic shielding efficiency results of r-PET and 20% mgt/r-PET samples in the range of 400 MHz to 6 GHz are shown in Figure 12.

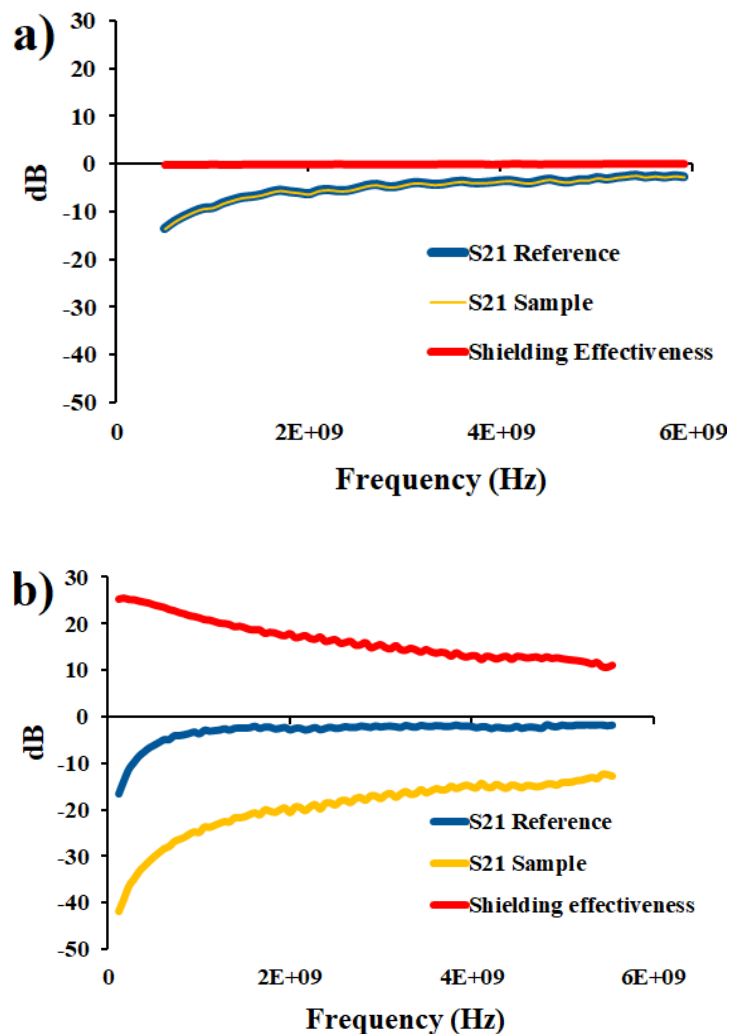


**Figure 12.** Electromagnetic shielding efficiency of (a) r-PET and (b) 20% mgt/r-PET samples (blue line: reference, yellow line: sample and red line: shielding efficiency)

r-PET itself did not exhibit any electromagnetic shielding. However, the addition of magnetite provided an efficiency of more than 22 dB which corresponded to around 99% shielding efficiency. With the combination of superhydrophobicity and icephobicity capability, the nanocomposite membranes could be suitable EMI shielding materials for outdoor applications (especially in cold climates).

There are three attenuation or loss mechanisms involved in EMI shielding: absorbance, reflectance, and multi-reflectance<sup>45</sup>. As reported previously, reflectance is the major attenuation mechanism when materials with high electrical conductivity and low magnetic

permeability are used, because of the impedance mismatch. However, impedance matching is required to design a good electromagnetic shielding absorber. EMI shielding property of the magnetite is already well reported in literature <sup>46-51</sup>. It is considered as a good electromagnetic absorber to satisfy the impedance matching condition. The absorption loss of magnetite composites is related to the thickness, dielectric constant, surface conductivity, permittivity, and permeability of the material. High magnetic permeability and high dielectric constant of magnetite makes it a promising material to fabricate polymer-based nanocomposites with high dielectric and magnetic permeability performance. Roberts et al. <sup>52</sup> reported that addition of magnetite in polymethylmethacrylate resulted in high permeability of polymer nanocomposite and increased multi-reflection loss. Prakash et al. found that the incorporation of magnetite provided high level of permittivity and permeability to natural rubber-based nanocomposites. Moreover, several works showed that magnetite is a promising material for high dielectric constant nanocomposites <sup>53, 54</sup>, which is another key advantage to achieve high electromagnetic absorption.

The main contribution to the microwave absorption capability of r-PET/magnetic nanofibre membrane was attributed by the ferromagnetic resonance which is coupling between the electromagnetic wave and the magnetization of the medium that it passes through. This effect reduces the power of the electromagnetic wave significantly and radiate small amount of heat. Moreover, the magnetite nanoparticles have a small coercivity value which is an important point for improving the permeability and hence, the magnetic loss. The schematic representation of the attenuation mechanism of a bulky regular EMI shielding material and an electrospun membrane is illustrated in Figure 13.

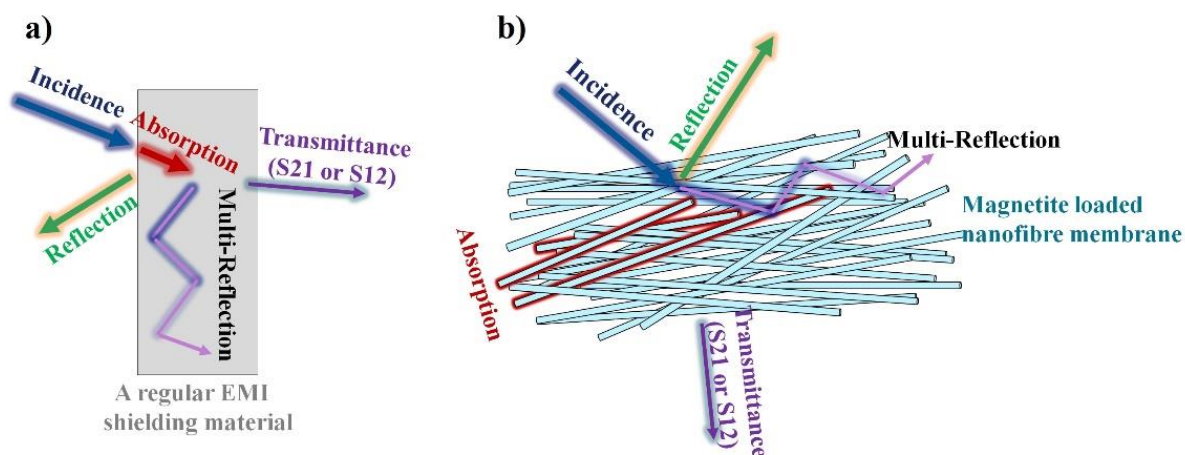


**Figure 13.** The schematic representation of the EMI shielding mechanisms using (a) a bulky regular EMI shielding material and (b) electrospun membranes.

The second influencing factor of the EMI shielding efficiency was the multi-reflection mechanism, in which the EMI waves are trapped between two boundaries<sup>55</sup> as indicated in Figure 13b. Therefore, the multi-reflection mechanism plays an important role in porous materials, for instance, the fibrous structures of electrospun membranes. For the attenuation mechanism of the electrospun membranes, the EMI waves are trapped between the nanofibres which leads to an increase in multi-reflectance loss. Additionally, the large specific surface area of the fibrous membranes may also affect the efficiency of EMI shielding. When the specific surface area of an EMI shielding material increases, the EMI shielding efficiency also increases. It is also noted that the addition of magnetite had impact on the fiber diameter distribution, resulting in higher surface area of electrospun membrane, which significantly affects the multi-reflection loss.

#### 4. Conclusions

In this study, icephobic nanocomposite electrospun membranes were developed via a two-step process from recycled polyethylene terephthalate (r-PET), which exhibited high electromagnetic shielding efficiency with superhydrophobic and icephobic performance. It was

found that 20 wt% magnetite loaded nanofibre membrane had an electromagnetic shielding efficiency of 22 dB, with EMI shielding efficiency above 99%. It is suggested that the fibrous structure of the electrospun membrane and the pores between the fibres contributed to the efficiency of 22 dB with the increasing multi-reflection loss. Moreover, a low ice adhesion strength compared with the aluminium substrates was obtained at around 50 kPa. Due to the icephobic and superhydrophobic performance, the prepared electrospun nanocomposite membranes have great potentials for outdoor EMI shielding applications, especially in cold regions.

**Corresponding Author:** Dr Xianghui Hou

E-mail: xianghui.hou@nottingham.ac.uk Tel: +44-115 95 13920

#### **Author Contributions**

The manuscript was written through contributions of all authors. All authors have given approval to the final version of the manuscript

#### **ACKNOWLEDGEMENT**

The authors would like to thank the Scientific and Technological Research Council of Turkey (TUBITAK) for providing financial support to Mahmut Tas with program number 2213, and the University of Nottingham Propulsion Futures Beacon for funding under Grant PF016/020. The authors also acknowledge the use of facilities at Nanoscale and Microscale Research Centre of the University of Nottingham, supported in part by the Engineering and Physical Sciences Research Council [grant number EP/L022494/1], and the Henry Royce Institute for the measurements of magnetic properties using SQUID.

#### **References**

1. Zamanian, A.; Hardiman, C., Electromagnetic radiation and human health: A review of sources and effects. *High Frequency Electronics* **2005**, 4 (3), 16-26.
2. Li, Y.; Chen, C. X.; Zhang, S.; Ni, Y. W.; Huang, J., Electrical conductivity and electromagnetic interference shielding characteristics of multiwalled carbon nanotube filled polyacrylate composite films. *Appl Surf Sci* **2008**, 254 (18), 5766-5771.

3. Lin, C. T.; Swanson, B.; Kolody, M.; Sizemore, C.; Bahns, J., Nanograin magnetoresistive manganite coatings for EMI shielding against directed energy pulses. *Prog Org Coat* **2003**, *47* (3-4), 190-197.
4. Yang, X.; Fan, S.; Li, Y.; Guo, Y.; Li, Y.; Ruan, K.; Zhang, S.; Zhang, J.; Kong, J.; Gu, J., Synchronously improved electromagnetic interference shielding and thermal conductivity for epoxy nanocomposites by constructing 3D copper nanowires/thermally annealed graphene aerogel framework. *Composites Part A: Applied Science and Manufacturing* **2020**, *128*, 105670.
5. von Klemperer, C. J.; Maharaj, D., Composite electromagnetic interference shielding materials for aerospace applications. *Compos Struct* **2009**, *91* (4), 467-472.
6. Geetha, S.; Kumar, K. K. S.; Rao, C. R. K.; Vijayan, M.; Trivedi, D. C., EMI Shielding: Methods and Materials-A Review. *Journal of Applied Polymer Science* **2009**, *112* (4), 2073-2086.
7. Mishra, R. K.; Thomas, M. G.; Abraham, J.; Joseph, K.; Thomas, S., Electromagnetic Interference Shielding Materials for Aerospace Application: A State of the Art. *Advanced Materials for Electromagnetic Shielding: Fundamentals, Properties, and Applications* **2018**, 327-365.
8. Ma, X. H.; Shen, B.; Zhang, L. H.; Liu, Y. F.; Zhai, W. T.; Zheng, W. G., Porous superhydrophobic polymer/carbon composites for lightweight and self-cleaning EMI shielding application. *Compos Sci Technol* **2018**, *158*, 86-93.
9. Das, A.; Hayvaci, H. T.; Tiwari, M. K.; Bayer, I. S.; Erricolo, D.; Megaridis, C. M., Superhydrophobic and conductive carbon nanofiber/PTFE composite coatings for EMI shielding. *Journal of Colloid and Interface Science* **2011**, *353* (1), 311-315.
10. Xing, Y. J.; Xue, Y. P.; Song, J. L.; Sun, Y. K.; Huang, L.; Liu, X.; Sun, J., Superhydrophobic coatings on wood substrate for self-cleaning and EMI shielding. *Appl Surf Sci* **2018**, *436*, 865-872.
11. Zou, L.; Lan, C. T.; Li, X. P.; Zhang, S. L.; Qiu, Y. P.; Ma, Y., Superhydrophobization of Cotton Fabric with Multiwalled Carbon Nanotubes for Durable Electromagnetic Interference Shielding. *Fiber Polym* **2015**, *16* (10), 2158-2164.
12. Han, J. T.; Kim, S. Y.; Woo, J. S.; Lee, G. W., Transparent, Conductive, and Superhydrophobic Films from Stabilized Carbon Nanotube/Silane Sol Mixture Solution. *Adv Mater* **2008**, *20* (19), 3724-+.
13. Zou, J. H.; Chen, H.; Chunder, A.; Yu, Y. X.; Huo, Q.; Zhai, L., Preparation of a superhydrophobic and conductive nanocomposite coating from a carbon-nanotube-conjugated block copolymer dispersion. *Adv Mater* **2008**, *20* (17), 3337-+.
14. Liu, L.; Xu, W.; Ding, Y.; Agarwal, S.; Greiner, A.; Duan, G., A review of smart electrospun fibers toward textiles. *Composites Communications* **2020**, *22*, 100506.
15. Tas, M.; Xu, F.; Ahmed, I.; Hou, X., One - step fabrication of superhydrophobic P (VDF - co - HFP) nanofibre membranes using electrospinning technique. *Journal of Applied Polymer Science* **2020**, *137* (24), 48817.
16. Zhang, Y.; Ruan, K.; Gu, J., Flexible Sandwich - Structured Electromagnetic Interference Shielding Nanocomposite Films with Excellent Thermal Conductivities. *Small* **2021**, *17* (42), 2101951.
17. Guo, H.; Chen, Y.; Li, Y.; Zhou, W.; Xu, W.; Pang, L.; Fan, X.; Jiang, S., Electrospun fibrous materials and their applications for electromagnetic interference shielding: A review. *Composites Part A: Applied Science and Manufacturing* **2021**, *143*, 106309.
18. Guo, H.; Wang, F.; Luo, H.; Li, Y.; Lou, Z.; Ji, Y.; Liu, X.; Shen, B.; Peng, Y.; Liu, K.; Jiang, S., Flexible TaC/C electrospun non-woven fabrics with multiple spatial-scale conductive frameworks for efficient electromagnetic interference shielding. *Composites Part A: Applied Science and Manufacturing* **2021**, *151*, 106662.
19. Tellli, A.; Ozdil, N., PROPERTIES OF THE YARNS PRODUCED FROM r-PET FIBERS AND THEIR BLENDS. *Tekstil Ve Konfeksiyon* **2013**, *23* (1), 3-10.
20. Tellli, A.; Ozdil, N., Effect of Recycled PET Fibers on the Performance Properties of Knitted Fabrics. *J Eng Fiber Fabr* **2015**, *10* (2), 47-60.

21. Mutsuga, M.; Tojima, T.; Kawamura, Y.; Tanamoto, K., Survey of formaldehyde, acetaldehyde and oligomers in polyethylene terephthalate food-packaging materials. *Food Addit Contam* **2005**, *22* (8), 783-789.
22. Hao, J. L.; Lei, G. T.; Li, Z. H.; Wu, L. J.; Xiao, Q. Z.; Wang, L., A novel polyethylene terephthalate nonwoven separator based on electrospinning technique for lithium ion battery. *J Membrane Sci* **2013**, *428*, 11-16.
23. Bishop, G.; Styles, D.; Lens, P. N., Recycling of European plastic is a pathway for plastic debris in the ocean. *Environment International* **2020**, *142*, 105893.
24. Peake, L., Plastic waste in the United Kingdom. In *Plastic Waste and Recycling*, Elsevier: 2020; pp 585-600.
25. Tas, M.; Memon, H.; Xu, F.; Ahmed, I.; Hou, X., Electrospun nanofibre membrane based transparent slippery liquid-infused porous surfaces with icephobic properties. *Colloids and Surfaces A: Physicochemical and Engineering Aspects* **2019**, 124177.
26. Xue, C. H.; Ji, P. T.; Zhang, P.; Li, Y. R.; Jia, S. T., Fabrication of superhydrophobic and superoleophilic textiles for oil-water separation. *Appl Surf Sci* **2013**, *284*, 464-471.
27. Laforte, C.; Beisswenger, A. In *Icephobic material centrifuge adhesion test*, Proceedings of the 11th International Workshop on Atmospheric Icing of Structures, IWAIS, Montreal, QC, Canada, 2005; pp 12-16.
28. Fortin, G.; Beisswenger, A.; Perron, J. In *Centrifuge adhesion test to evaluate icephobic coatings*, AIAA Atmospheric and Space Environments Conference, 2010; p 7837.
29. Liu, J. P.; Janjua, Z. A.; Roe, M.; Xu, F.; Turnbull, B.; Choi, K. S.; Hou, X. H., Super-Hydrophobic/Icephobic Coatings Based on Silica Nanoparticles Modified by Self-Assembled Monolayers. *Nanomaterials-Basel* **2016**, *6* (12).
30. Vasquez, H.; Espinoza, L.; Lozano, K.; Foltz, H.; Yang, S., Simple device for electromagnetic interference shielding effectiveness measurement. *IEEE EMC Soc. Newslett* **2009**, *220*, 62-68.
31. Fridrikh, S. V.; Yu, J. H.; Brenner, M. P.; Rutledge, G. C., Controlling the fiber diameter during electrospinning. *Phys Rev Lett* **2003**, *90* (14).
32. Das, G.; Mariotto, G.; Quaranta, A., Microstructural evolution of thermally treated low-dielectric constant SiOC : H films prepared by PECVD. *J Electrochem Soc* **2006**, *153* (3), F46-F51.
33. Shokri, B.; Firouzjah, M. A.; Hosseini, S. I. In *FTIR analysis of silicon dioxide thin film deposited by metal organic-based PECVD*, Proceedings of 19th international symposium on plasma chemistry society, Bochum, Germany, 2009.
34. Ignat'eva, L. N.; Buznik, V. M., IR-spectroscopic examination of polytetrafluoroethylene and its modified forms. *Russ J Gen Chem+* **2009**, *79* (3), 677-685.
35. Van Krevelen, D. W.; Te Nijenhuis, K., *Properties of polymers: their correlation with chemical structure; their numerical estimation and prediction from additive group contributions*. Elsevier: 2009.
36. Wei, D. W.; Wei, H.; Gauthier, A. C.; Song, J.; Jin, Y.; Xiao, H., Superhydrophobic modification of cellulose and cotton textiles: Methodologies and applications. *Journal of Bioresources and Bioproducts* **2020**, *5* (1), 1-15.
37. Azimi, A.; He, P., Effect of gravity in the Cassie-to-Wenzel transition on a micropatterned surface. *Mrs Commun* **2020**, *10* (1), 129-134.
38. Sojoudi, H.; Wang, M.; Boscher, N.; McKinley, G. H.; Gleason, K. K., Durable and scalable icephobic surfaces: similarities and distinctions from superhydrophobic surfaces. *Soft matter* **2016**, *12* (7), 1938-1963.
39. Subramanyam, S. B.; Kondrashov, V.; Ruhe, J.; Varanasi, K. K., Low Ice Adhesion on Nano-Textured Superhydrophobic Surfaces under Supersaturated Conditions. *Acs Applied Materials & Interfaces* **2016**, *8* (20), 12583-12587.
40. Kulinich, S. A.; Farzaneh, M., How Wetting Hysteresis Influences Ice Adhesion Strength on Superhydrophobic Surfaces. *Langmuir* **2009**, *25* (16), 8854-8856.
41. Fu, Q.; Wu, X.; Kumar, D.; Ho, J. W.; Kanhere, P. D.; Srikanth, N.; Liu, E.; Wilson, P.; Chen, Z., Development of sol-gel icephobic coatings: effect of surface

- roughness and surface energy. *ACS applied materials & interfaces* **2014**, 6 (23), 20685-20692.
42. Kulinich, S.; Farzaneh, M., How wetting hysteresis influences ice adhesion strength on superhydrophobic surfaces. *Langmuir* **2009**, 25 (16), 8854-8856.
43. Sojoudi, H.; McKinley, G. H.; Gleason, K. K., Linker-free grafting of fluorinated polymeric cross-linked network bilayers for durable reduction of ice adhesion. *Materials Horizons* **2015**, 2 (1), 91-99.
44. Farhadi, S.; Farzaneh, M.; Kulinich, S. A., Anti-icing performance of superhydrophobic surfaces. *Appl Surf Sci* **2011**, 257 (14), 6264-6269.
45. Al-Saleh, M. H.; Sundararaj, U., Electromagnetic interference shielding mechanisms of CNT/polymer composites. *Carbon* **2009**, 47 (7), 1738-1746.
46. Crespo, M.; Mendez, N.; Gonzalez, M.; Baselga, J.; Pozuelo, J., Synergistic effect of magnetite nanoparticles and carbon nanofibres in electromagnetic absorbing composites. *Carbon* **2014**, 74, 63-72.
47. Nasouri, K.; Shoushtari, A. M., Fabrication of magnetite nanoparticles/polyvinylpyrrolidone composite nanofibers and their application as electromagnetic interference shielding material. *J Thermoplast Compos* **2018**, 31 (4), 431-446.
48. Chiscan, O.; Dumitru, I.; Postolache, P.; Tura, V.; Stancu, A., Electrospun PVC/Fe<sub>3</sub>O<sub>4</sub> composite nanofibers for microwave absorption applications. *Mater Lett* **2012**, 68, 251-254.
49. Guo, J.; Song, H. X.; Liu, H.; Luo, C. J.; Ren, Y. R.; Ding, T.; Khan, M. A.; Young, D. P.; Liu, X. Y.; Zhang, X.; Kong, J.; Guo, Z. H., Polypyrrole-interface-functionalized nano-magnetite epoxy nanocomposites as electromagnetic wave absorbers with enhanced flame retardancy. *J Mater Chem C* **2017**, 5 (22), 5334-5344.
50. Al - Ghamdi, A.; Al - Hartomy, O. A.; Al - Salamy, F.; Al - Ghamdi, A. A.; El - Mossalamy, E.; Abdel Daiem, A.; El - Tantawy, F., Novel electromagnetic interference shielding effectiveness in the microwave band of magnetic nitrile butadiene rubber/magnetite nanocomposites. *Journal of applied polymer science* **2012**, 125 (4), 2604-2613.
51. Posada, A. O. G.; Téllez, D. A. L.; Roa-Rojas, J.; Barrado, J. R. R., Electromagnetic shielding response of magnetite elastomeric composites: Source and filler content dependence. *Journal of Materials Research and Technology* **2020**, 9 (5), 10597-10607.
52. Sharif, F.; Arjmand, M.; Moud, A. A.; Sundararaj, U.; Roberts, E. P., Segregated hybrid poly (methyl methacrylate)/graphene/magnetite nanocomposites for electromagnetic interference shielding. *ACS applied materials & interfaces* **2017**, 9 (16), 14171-14179.
53. Tsonos, C.; Zois, H.; Kanapitsas, A.; Soin, N.; Siores, E.; Peppas, G.; Pyrgioti, E.; Sanida, A.; Stavropoulos, S.; Psarras, G., Polyvinylidene fluoride/magnetite nanocomposites: Dielectric and thermal response. *Journal of Physics and Chemistry of Solids* **2019**, 129, 378-386.
54. Maharramov, A.; Ramazanov, M.; Palma, L.; Shirinova, H.; Hajiyeva, F., Influence of Magnetite Nanoparticles on the Dielectric Properties of Metal Oxide/Polymer Nanocomposites Based on Polypropylene. *Russian Physics Journal* **2018**, 60 (9).
55. Shukla, V., Review of electromagnetic interference shielding materials fabricated by iron ingredients. *Nanoscale Advances* **2019**, 1 (5), 1640-1671.